Chemical durability and corrosion-induced microstructure evolution of compositionally complex titanate pyrochlore waste forms with uranium incorporation

Kun Yang[1], Keith Bryce[1], Tiankai Yao,[2] Dong Zhao[1], Jie Lian[1,3]*

[1]*Department of Mechanical, Aerospace and Nuclear Engineering, Rensselaer Polytechnic Institute, NY, US, 12180*

[2]*Idaho National Laboratory, Idaho Falls, ID*

[3]*Department of Materials Science & Engineering, Rensselaer Polytechnic Institute, NY, US, 12180*

* Corresponding author, Email: lianj@rpi.edu; Office: 518-276-6081; Fax: 518-276-6025

Chemical durability of compositionally-complex rare-earth titanate pyrochlore solid solutions with or without uranium incorporation were investigated by semi-dynamic leaching testing. A Ti-enriched amorphous passivation film covered on surface due to the surface alteration-reorganization mechanism with preferential release of the weakly oxygen-bonded rare earth elements. Elemental release is found to be strongly correlated with chemical disorder, with a negligible correlation with entropy. The release rate of the uranium gradually decreases with increasing numbers of components, implying a possibility of designing and optimizing waste form performance with enhanced chemical durability by controlling composition complexity and chemical disorder for effective nuclear waste management.

1 Introduction

The safe disposal of nuclear wastes including fission products, U, Pu and minor actinides generated by commercial reactors and dismantled nuclear weapons has long been a major subject for effective nuclear waste management [1,2]. Significant efforts have been developed to immobilize nuclear waste in highly stable and durable host matrices, including SYNROC, apatite, vanadate, perovskite, and pyrochlore, *etc* [3-10]. Among these conventional nuclear waste forms, rare earth titante and zirconate pyrochlores ($A_2B_2O_7$ with A = REE, B = Ti and Zr) have been widely recognized as important host matrices in immobilizing nuclear waste due to their structural flexibility that can accommodate U, Pu and minor actinides with multiple valence states [11,12]. Pyrochlore structure types also possess diverse crystal chemistry and tunable structures with different combinations of elemental substitutions at the A and B-sites [11,16,17]. Besides, pyrochlore-type ceramics are also potential inert matrix fuels to incorporate multivalent uranium, plutonium, and transuranic actinides [2,12].

An order-disorder structural transition can occur in pyrochlore structure by disordering cation and anion sublattices, leading to the phase transformation from the ordered pyrochlore to a defect fluorite structure which can be induced by chemical substitution, temperature and intense beam irradiation [18-22]. The tendency towards the pyrochlore-to-fluorite phase transformation is dictated by the ionic radius ratio of cations at the A- and B-sites, which play a dominant role in controlling radiation tolerance and corrosion resistance of materials. In addition to host phases for nuclear waste management and inert matrix fuels, rare earth zirconate pyrochlores $Re_2Zr_2O_7$ are

also leading materials for thermal barrier coatings to enhance the operation temperature and increase longevity of the structural components for aerospace and space applications [23-25]. The phase and structural stability, chemical durability and oxidation/corrosion resistance of the pyrochlore structural types are essential for the evaluation of their performance as leading candidate materials for nuclear waste forms, inert matrix fuels and thermal barrier coatings in which materials are utilized either in separate or coupled extremes of high temperature, oxidative and corrosion environments.

Recently, high-entropy ceramics (HECs) has been emerging as a new class of materials with unique properties as compared with monolithic and single component materials resulting from their composition complexity, structural disordering and reduced atomic and thermal transport behavior. High entropy ceramics including boride, carbide, phosphate, silicate etc. attract great scientific interests due to their improved thermal and mechanical properties [14,15]. Multi-principal ceramics (MPCs) extended to both medium-entropy and non-equiatomic compositions may demonstrate excellent mechanical strength and ductility, significantly-lower thermal conductivity, superior corrosion resistance, and radiation tolerance. Multicomponent and high entropy ceramics may possess immense potentials with extended performance when utilized under extreme environments encountered for advanced nuclear energy systems and space/aerospace applications in which high thermo-mechanical properties, robust radiation tolerance, and high-temperature oxidation/corrosion are desirable [13,14].

Compositionally complex oxide solid solutions in pyrochlore and fluorite structures with varied A and B-site cationic combinations have been successfully fabricated, and their thermo-mechanical properties have been investigated systematically in order to understand the key materials parameters (such as size disorder, mass disorder, entropy, etc.) governing their properties. For example, Luo (2021) and Wright (2021) fabricated compositionally complex pyrochlore or fluorite solid solutions and high-entropy ceramics exhibiting superior low thermal conductivity and high mechanical strength [14,15]. A synergistic effect of the oxygen vacancies and the size disorder in influencing the thermal conductivities in compositionally complex fluorite and pyrochlore oxides was reported. It has also been reported that the chemical disorder instead of high entropy actually plays a dominant role in controlling their thermal-mechanical properties. Particularly, medium entropy pyrochlore solid solutions outperform their high-entropy counterparts with significantly lower thermal conductivity and better mechanical strength [14,15], desirable for the application of thermal/environmental barrier coatings. Similarly, titanate pyrochlore solid solutions from binary, multicomponent to high entropy materials containing with or without uranium have also been fabricated [23] in order to explore their potential applications as nuclear waste forms and inert matrix fuels. It was found that binary titanate pyrochlore solid solutions with uranium incorporation exhibit lower thermal conductivity and higher hardness, while a high entropy titanate pyrochlore solid solution $(Sm,Gd,Dy,Er,Yb,U)_2Ti_2O_7$ demonstrates higher thermal conductivity [26]. A close correlation

79 can be identified in the thermal conductivity with the size disorder and mixing entropy for
80 multicomponent titanate pyrochlores as demonstrated by our previous research [26]. Therefore,
81 the thermal and mechanical properties can be tailored by controlling its chemical disorder
82 associated with the compositional complexity, greatly expanding the design window to develop
83 high performance materials for both thermal barrier coatings and engineering materials for
84 nuclear applications [26].

85 This work mainly deals with the chemical durability and corrosion resistance of the
86 multicomponent titanate pyrochlore as potential nuclear waste forms and their microstructure
87 evolution under near field environment. We hypothesized that the chemical durability and
88 corrosion resistance of pyrochlore or fluorite structure types may also be impacted significantly
89 by the chemical disorder and composition complexity. A systematic study on single component
90 rare earth pyrochlore or fluorite demonstrates a clear trend of the elemental release rates
91 decreasing with the smaller A-site ionic radii from La to Yb [27,28]. A previous study by Xu
92 (2004) studied the chemical durability of a natural pyrochlore mineral $CaU_{0.5}Ce_{0.25}Hf_{0.25}Ti_2O_7$,
93 essentially a multicomponent crystalline solid solution [7], and the long-term uranium release
94 rate was around 10^{-5} g $m^{-2}\cdot d^{-1}$ in an acidic solution with pH = 2.0, demonstrating its excellent
95 long-term chemical durability [29]. However, mechanistic understanding is limited in the
96 chemical durability and corrosion resistance of compositionally complex pyrochlore and fluorite
97 solid solutions. As inspired by the greatly improved thermal and mechanical properties of the

compositionally complex pyrochlore solid solutions, it is possible to design advanced waste form materials with enhanced chemical durability and corrosion resistance based on multicomponent pyrochlore solid solutions by controlling its chemical disorder and structural distortion associated with the compositional complexity.

To test our hypothesize and design advanced waste form materials with optimized chemical stability and corrosion resistance, in this work, multicomponent titanate pyrochlore solid solutions with or without uranium incorporation were fabricated, and their chemical durability was evaluated in order to develop and understand the underlying mechanism that governs the chemical durability of the compositionally complex pyrochlore solid solutions. A systematic investigation of the corrosion behavior and degradation in aqueous solution in the near field environment was conducted, and their structural characteristics and properties were compared with multicomponent pyrochlore compositions without uranium. Specifically, a total of 9 pyrochlore compositions from binary, ternary, and quaternary to five-components with and without uranium incorporation were synthesized, corresponding to low entropy, medium entropy and high entropy materials. The short-term and long-term elemental release rates were further determined by solution chemistry analysis using an inductively-coupled plasma mass spectroscopy (ICP-MS). The chemical durability of the compositionally complex pyrochlore solid solutions was linked with structural/chemical disorder in order to reveal the dominant mechanisms in guiding the design and optimization of multicomponent oxide solid solutions and

predicting their performance under the near field environment for waste form applications.

2 Materials and Methods

2.1 Powder Fabrication

Multicomponent or high-entropy pyrochlores can be synthesized via wet chemical approaches such as sol-gel processing, hydrothermal route, co-precipitation, polymeric Pechini method and pyrolysis of aerosols [30-32]. These methods usually require a long dwell time with relatively high temperatures, and it is difficult to control the phase purity due to the addition of precipitation agents for the wet chemical approaches [33-35]. Therefore, in this work, multicomponent titanate pyrochlore solid solutions were synthesized by solid state reaction of the precursor chemicals (RE_2O_3 and TiO_2) through high-energy ball milling. Multicomponent $REE_2Ti_2O_7$ with different combinations of rare-earth elements varying from Sm to Yb were targeted to represent medium to high entropy materials. In addition, the $REE_2Ti_2O_7$ (REE = Sm to Yb) solid solutions with 5 at.% uranium incorporation into the structural lattice (target formula of $REE_{1.95}U_{0.05}Ti_2O_7$) were also fabricated using UO_2 as the precursor chemical. The amount of UO_2 was deliberately selected as 5 at.% based on our previous research, which suggested that the maximum 10 at% UO_2 can be incorporated into the pyrochlore lattice structure [26]. Above 10 at%, a secondary phase, namely U_3O_8 can be found for the pyrochlore sample. The REE_2O_3, UO_2, and TiO_2 powders were thermally pre-treated in a digitally-controlled oven at 500 ^oC for 24 hours in order to remove adsorbed moisture. Stoichiometric amounts of the precursor materials (about 5

grams) were mixed in 10 ml pure ethanol with a solid weight/liquid volume (w/v) ratio of 1 to 2. The mixed powders were then ball-milled for 80 cycles at 500 rpm with ZrO_2 milling apparatus, for which each cycle was equal to 30 min with a pause of 5 min between each cycle to prevent the mixture solution from overheating. The ball milling was conducted with high-energy ball milling equipment (FRITSCH). After the ball milling, the mixture slurry was then dried for 24 hours in the air at 90 °C to remove any remaining ethanol.

Table 1. Target chemical formula of the samples studied herein

No.	A-site (at.%)						B-site (at.%)	chemical composition
	Sm_2O_3	Gd_2O_3	Dy_2O_3	Er_2O_3	Yb_2O_3	UO_2	TiO_2	
1	25	0	0	0	25	0	50	$(Sm,Yb)_2Ti_2O_7$
2	16.7	16.7	0	0	16.7	0	50	$(Sm,Gd,Yb)_2Ti_2O_7$
3	12.5	12.5	0	12.5	12.5	0	50	$(Sm,Gd,Er,Yb)_2Ti_2O_7$
4	10	10	10	10	10	0	50	$(Sm,Gd,Dy,Er,Yb)_2Ti_2O_7$
5	0	0	0	0	45	5	50	$(Yb,U)_2Ti_2O_7$
6	22.5	0	0	0	22.5	5	50	$(Sm,Yb,U)_2Ti_2O_7$
7	15	15	0	0	15	5	50	$(Sm,Gd,Yb,U)_2Ti_2O_7$
8	11.3	11.3	0	11.3	11.3	5	50	$(Sm,Gd,Er,Yb,U)_2Ti_2O_7$
9	9	9	9	9	9	5	50	$(Sm,Gd,Dy,Er,Yb,U)_2Ti_2O_7$

2.2 Pellet Sintering

The targeted pyrochlore solid solutions in dense ceramic pellets were consolidated by spark plasma sintering (SPS) using a Model 10-3 SPS system (Thermal Tech, LLC, Santa Rosa, California). A portion of 0.75 g of the dried powders was consolidated with an 8 mm graphite die. Graphite foils sprayed with boron nitride paste were placed between the graphite die and the

149 powder compact to act as a physical barrier (thickness around 0.2 mm). A thick graphite coat
150 surrounded the graphite die was applied to prevent over-heat loss during the sintering process. A
151 steady flow of argon gas with the flow rate of 1 L/min passed through the chamber during SPS
152 sintering. The sintering temperature was monitored and controlled using a pyrometer. The
153 sintering temperature was increased from 25 to 1250 ºC with a heating rate of 200 ºC/min, and
154 the uniaxial pressure was increased to 40 MPa simultaneously. The maximum temperature and
155 pressure were held for 15 min to allow the grain coarsening and densification. After the thermal
156 holding period, the graphite die and sintered pellets were cooled down with a continuous argon
157 gas flow (1 L/min) to room temperature. The as-sintered pellets were first roughly polished by
158 1200 grit sandpapers with water acting as the polishing agent, then deeply polished and finished
159 using 1 μm diamond paste and 0.03 μm silica gel paste. Sample pellets were then rinsed and
160 cleaned with deionized water in an ultrasonic cleaner. The density of sintered pellets was
161 measured based on Archimedes method using an Adam analytical scale (Danbury, NY, USA).

162 **2.3 Phase and microstructure characterization**

163 The phase of the densified pellets obtained after final polishing was characterized by X-ray
164 diffraction (XRD) using a Panalytical X'Pert Pro system. The scanning ranges from 10º to 90º
165 (Westborough, MA, USA) along with a copper target ($CuK_{\alpha I}$= 0.15406 nm, $CuK_{\alpha II}$= 0.15443 nm)
166 and a step size of 0.0131º. The surface microstructure before and after the chemical durability test
167 by leaching in nitric acid solutions (pH = 1) was characterized using a scanning electron

168 microscope (SEM) equipped with an energy dispersive spectroscope (EDS) (FEI Versa, USA).
169 The properties of the chemical bonding environment of the as-sintered pellets before and post
170 accelerated leaching tests were further characterized by Raman spectroscopy (using a Renishaw
171 system, model DXR2). The surface morphology and microstructure evolution and corresponding
172 semi-quantitative elemental analysis were characterized using a scanning transmission electron
173 microscopy (STEM, FEI Titan Model 80-200, USA) system coupled with an energy dispersive
174 spectroscope (EDS, Oxford Instruments, Abingdon, UK). Samples for analysis by STEM were
175 prepared by a focused ion beam (FIB) (FEI Versa, USA) to obtain thin lamellas with the
176 thickness to 50 nm. A 100 nm Pt protection layer was coated onto the cutting area to avoid
177 possible beam damage and artifacts on the ceramic surface.

178 **2.4 Semi-dynamic leaching test**

179 Short-term (1-day) and long-term (14-day) semi-dynamic leaching tests were carried out in
180 (18 Ω) deionized water solution with pH =1.0 using highly purified nitric acid following an
181 accelerated leaching method ASTM C1308 standard test [34]. Aggressive leaching experiments
182 were conducted at 90 °C in a cap-covered PTFE vessel in a digitally controlled oven. The
183 leachates were sampled and exchanged for 3 hours intervals for the first 24 hours short-term
184 period and a 1-day interval for the long-term leaching period until 14-days. The sample's surface
185 area/leachate volume (S/V) ratio was kept at 5.0 throughout the experiment, and the elemental
186 release rates were analyzed using an ICP-MS (Varian 820, California, US). The corresponding

187 leaching rates (as $mg \cdot m^{-2} \cdot hr^{-1}$) or ($mg \cdot m^{-2} \cdot d^{-1}$), were calculated according to equation (1):

188 $$m(i) = \frac{C_i V}{ST} \quad (1)$$

189 in which C_i is the concentration measured with ICP-MS in milligrams per liter, V is the leachate
190 volume in liters, and S is the surface area in square meters and T stands for the sampling interval
191 which equals to 3 hours for first 24 hours and 1-day from day-2 to day-14. The value of S/V was
192 assumed to be consistent during the leaching experiment (S/V = 5.0).

193 The initial or short-term rates (as $mg \cdot m^{-2} \cdot d^{-1}$) were obtained by averaging the leaching rates
194 within 24 hours by assuming that the initial leaching was regulated by the dissolution mechanism.
195 The long-term rate (as $mg \cdot m^{-2} \cdot d^{-1}$) was calculated based on the modified Cote's model [37],
196 assuming that the long-term leaching behavior was dominated by the dissolution and diffusion
197 mechanisms only:

198 $$m(t) = k_1 t + k_2 t^{1/2} + k_3 (1 - e^{-k_4 t}) \quad (2)$$

199 The Cote's model is a semi-empirical mathematical model designed to explain surface
200 leaching behavior by considering dissolution, surface effect and diffusion [34]. The first term, $k_1 t$,
201 on the equation (2) represents the linear dissolution behavior, while the second term stands for
202 the mass transport by diffusion [37], and the third part represents the dissolution behavior
203 dominated by surface ion-exchange. The short-term rate can be derived by assuming a constant
204 initial fast dissolution rate, while the long-term rate can be determined by assuming infinite
205 leaching time and the long-term behavior is dominated by dissolution and diffusion without

surface effects, and the long-term dissolution rate can be approximated by k_1.

3 Results and Discussion

3.1 Surface morphology and phase of the as-sintered pellets

The XRD patterns for the as-sintered multicomponent pyrochlore solid solutions can be seen in Figure 1a-b and the calculated lattice constant is shown in supplemental Figure s1. Results denote the highly crystallized cubic pyrochlore structure dominating in the multicomponent pyrochlore solid solutions with superlattice diffraction peaks indexed as (111), (222) and (331) of the ordered pyrochlore structure. The XRD patterns for the uranium-incorporated pyrochlore solid solutions do not show impurity phases, indicating that the 5 at.% uranium was successfully incorporated into the pyrochlore lattice structure by partially substituting the A-site in the lattice structure without phase segregation, consistent with our previous study [26]. The lattice constants vary from 10.04 to 10.2 angstrom for the cubic pyrochlore structure based on the Rietveld refinement. The lattice expansion can be observed for the $(Yb,U)_2Ti_2O_7$ as compared to $Yb_2Ti_2O_7$ as confirmed by our previous research due to the incorporation of uranium [26]. Figure 1c shows the surface morphology and corresponding elemental distributions of the uranium-incorporated high-entropy pyrochlore. The SEM image shows that the as-sintered pellets are highly densified without manifest porosity, and multicomponent elements including uranium are homogeneously distributed without phase segregation or agglomeration.

Raman microscopy has been used as a powerful approach to characterize the chemical

bonding of pyrochlore materials [38]. The as-sintered pyrochlore solid solutions were characterized by Raman spectroscopy under ambient conditions to better understand the structural evolution before and post leaching test, as shown in Figure 2b. The pyrochlore structure belongs to the $Fd\bar{3}m$ space group and has six Raman active modes in the center of the Brillouin zone: $\Gamma = A_{1g} + E_g + 4F_{2g}$, according to the group theory [38]. The pyrochlore solid solutions studied herein all exhibit three typical vibration modes in the range of 200-800 cm^{-1}, namely, A_{1g}, E_g and F_{2g}, with no other vibration modes, suggesting a high purity pyrochlore phase [39-41]. The most intensive Raman peak vibration around 306 cm^{-1} corresponds to the E_g mode which is related to the Ti-O bending vibration. The band at around 520 cm^{-1} corresponds to the A_{1g} mode and is related to the O-Ti-O bending vibration of the TiO_6 octahedron. The band at 580 cm^{-1} corresponds to the F_{2g} vibration mode and is related to the Ti-O stretching vibration [39-41]. Detailed analysis was carried out by a Gaussian fit of the Raman peaks, as shown in Figure 2 and the corresponding peak positions are summarized in supplemental Figure S1b. It can be observed that three Raman modes move to higher frequency (blue shift) from $(Sm,Gd,Yb)_2Ti_2O_7$ to high entropy ceramics (HEC(5)), corresponding to the decrease of average ionic radii and the strengthening of the corresponding chemical bond [40,41]. It is worthy of noting that the shift of Raman modes and the shift of X-ray diffraction peaks show a very similar tendency, further suggesting that the blue shift of the Raman modes is accompanied with the decrease in lattice parameters.

3.2. Microstructure evolution and surface alteration of the pyrochlore solid solutions after leaching

The surface microstructure and morphology evolution of the pyrochlore solid solution samples post 14-days leaching are shown in Figure 2a, while the surface structure of the as-fabricated samples can be seen in the Supplemental Information Figure s3. The original surface structure is not visible due to the formation of a dense passivation film on the leached surfaces for the samples with or without uranium post the 14-days' alteration in a nitric acid solution. The dense passive film is composed of nano-sized alteration products with irregular structure and average grain size around 20 nm homogeneously, similar to the observation on the single component pyrochlores reported previously [27,28]. The surface alteration of the high entropy pyrochlore solid solution $(Sm,Gd,Dy,Er,Yb)_2Ti_2O_7$ post 14-days' leaching test was further characterized by Raman spectroscopy as shown in Figure 2c. Compared to the as-fabricated sample pellet, peak intensities of the F_{2g} are significantly increased after 14-day's leaching period, suggesting significant changes in the structure of corroded materials with an enhancement of the Ti-O stretching band. The increase of the Ti-O stretching mode intensity might suggest the surface passivation film with a chemical composition featured by a Ti-enriched layer. The Ti-enriched surface passivation film can be further evidenced by the STEM analysis.

In order to understand the impact of dissolution on surface alteration and passivation film formation on high-entropy Ti-pyrochlore, STEM study was carried out on the cross-section of the leached sample of $(Sm,Gd,Dy,Er,Yb)_2Ti_2O_7$ and the results are shown in Figures 3 and 4. The

alteration zone of 50 nm underneath the Pt protective layer can be seen in Figure 3a and the high-resolution image in Figure 3c. A 25 nm thick passivation film featured by both the amorphous and fluorite structure coves on the altered matrix, as evidenced by the FFT of the image showing bright diffraction spots and amorphous hallow rings (see Figure 3c). The nano-sized particles embedded in the amorphous passivation film maintain a fluorite structure as shown by the bright spots in Fourier-transferred image (FFT) (Figure 3f). The altered matrix underneath demonstrates an ordered pyrochlore structure, as evidenced by the existence of the superlattice in the FFT pattern (Figure 3e). The high resolution TEM image (Fig. 3b) and the SAED (Fig. 3e) view along a zone axis of [110] show a perfect pyrochlore superstructure for the original unaltered matrix beneath the altered matrix.

The cross-sectional microstructure and elemental line scanning across on the alteration zone of HEC with U incorporation (HEC(U)) are shown in Figure 4. The surface passivation layer with a thickness of around 25 nm with a coexisted of amorphous and disordered fluorite structure can be evidenced by the HAADF image in Figure 4b, consistent with the STEM analysis in Figure 3. The elemental line scanning focused on the passivation film and the altered matrix clearly indicates that the passivation film is enriched with Ti but depleted with rare earth elements, and the atomic ratio of REE/Ti is significantly below the stoichiometric ratio of 1.0 for high entropy titanate pyrochlore. The Ti-enriched passivation film display the amorphous feature, implying that the formation of the surface passivation film might be dominated by a surface

283 alteration-reorganization mechanism instead of dissolution-reprecipitation mechanism [42]. The
284 preferential release of rare earth elements from weakly-bonded REE-O followed by a
285 reorganization of the surface alteration layer enriched with the strongly-bonded Ti, lead to the
286 formation of the passivation film. The surface alteration and reorganization mechanism has been
287 previously applied to explain the formation of passivation films in borosilicate glass and
288 titanate-based ceramics, *e.g.*, $CaTiO_3$ [43]. The formation of the Ti-enriched amorphous layer was
289 also reported for the U-bearing natural pyrochlore post long-term dissolution though the
290 formation mechanism of the amorphous film was not discussed [42].

291 **3.3 Chemical durability and semi-dynamic leaching of pyrochlore solid solutions**

292 The chemical durability of the as-sintered titanate pyrochlore solid solutions was evaluated
293 through semi-dynamic leaching tests in nitric acid (pH = 1, 90 ^{o}C) for 14-days. The normalized
294 leaching rates corresponding to the A-site elements are shown in Figures 5 and 6. The short-term
295 elemental release rates can be calculated by assuming that the initial dissolution mechanism is
296 dominated by a constant elemental release rate within the first 24 hours. The long-term elemental
297 release rates can be further determined by fitting the elemental release curve with the Cote's
298 model (the fitting parameters summarized in Supplemental Table S1.

299 In general, no significant difference in the element release rates for lanthanide elements at
300 the A-site except Gd can be observed regardless their compositions. Interestingly, Gd has the
301 lowest release rate among the A-site elements from Sm to Yb for the multicomponent solid

solutions without uranium incorporation. This is in drastically different to the single component Ti-pyrochlore as reported previously [27,28], in which the A-site elemental release rate increases from Yb to La with larger ionic radii of lanthanides and reduced metal-oxygen (A-O) bonding strength [27,43]. By forming multicomponent solid solutions, the leaching rates of large ionic-sized Sm and Gd are greatly suppressed by the structural and chemical disorder accompanying with the increase of the dissolution rate for smaller-sized lanthanides such as Dy, Er and Yb. The similar leaching rates in the binary and multicomponent solid solutions among different rare-earth elements observed here implies a similar bond environment for lanthanides in the solid solutions. A similar phenomenon can also be observed for the uranium-incorporated titanate pyrochlore solid solutions, and the rare earth elemental release rates are among the same order of magnitude.

The elemental release rates in general for each major element decreases accordingly with the increased numbers of component in the solid solution, suggesting improved chemical durability of materials from the binary $(Sm,Yb)_2Ti_2O_7$ to high-entropy ceramics $(Sm,Gd,Dy,Er,Yb,U)_2Ti_2O_7$. In addition, the normalized uranium release rate is significantly reduced from binary to high-entropy uranium-incorporated titanate pyrochlore solid solutions, as shown in Figure 7a, with the lowest normalized long-term uranium release rate around 10 $mg_N \cdot m^{-2}d^{-1}$ in nitric acid solution at pH=1 for HEC(U). The greatly improved corrosion resistance of the high entropy materials as evaluated by the release rate of uranium can be

attributed to the synergistic effect of strong chemical disorder and surface passivation resulting from the surface alteration-reorganization.

3.4. Dissolution mechanisms of the compositionally complex pyrochlore solid solutions

The leaching mechanism changes from incongruent dissolution to congruent dissolution and then to incongruent dissolution, which can be clearly evidenced by the change in the atomic ratio (A/Ti) in leachate (shown in Figs. 7b). Specifically, the atomic ratio of $(Sm,Yb)_2Ti_2O_7$ is well-below 1.0, suggesting a preferentially release of Ti than A-site element, consistent with our previous observation for the single component pyrochlore with smaller-sized lanthanide (e.g., $Er_2Ti_2O_7$ or $Yb_2Ti_2O_7$). The preferential release of Ti might be attributed to the metal-bond strength itself, and we hypothesize that the incorporation of the smaller-sized lanthanide, e.g., Yb or Er into the pyrochlore structure, not only alters the bond strength of the A-O polyhedron but also the bonding environment of the Ti-O octahedral. This results in the variation of their relative bond strengths and thus resistance against bond-breaking with aqueous corrosion. However, how the chemical disorder impact the bonding environment needs a thoroughly characterization of their bond strength. From the A/Ti ratio shown in Fig. 7b, the incorporation of large-sized REE elements into multicomponent solid solution leads to the preferential release of A-site elements, with the atomic ratio of A/Ti gradually increasing and higher than 1.0 for the ternary and quaternary compositions and then reduced for the high entropy ceramics, as shown in Figure 7b. The change in the corrosion mechanisms from incongruent dissolution to congruent and then

back to incongruent dissolution is also consistent with our previous observation of the single component rare earth titanate and zirconate pyrochlores [27,28]. These results suggest complex dissolution behavior and corrosion mechanisms, and the underlying dominated mechanism will be further discussed in the next section.

Similar to the single component Ti-pyrochlore previously studied [27,28], the short-term and long-term dissolution kinetics of the as-sintered pyrochlore solid solution are obtained and elaborated in Figures 7c-d for the multicomponent compositions with or without uranium incorporation. Three different stages can be classified in terms of the dissolution kinetics based on the transition stage theory (TST) [44]: (1) matrix dissolution, (2) transition stage and (3) diffusion dominated long term dissolution. According to the TST theory, the crystals with defects such as dislocations can dissolve rapidly [45], which can be attributed to either surface defects and edge dislocations as a result of significantly high surface energy or chemical inhomogeneity, resulting in rapid release from these energetically favorable sites [46,47]. After the first 3 hrs with rapid initial matrix dissolution, a constant dissolution rate can be observed for the leaching up to 24 hrs, corresponding to the rate plateau for crystal dissolution far from equilibrium condition without solution feedback for semi-dynamic leaching experiments. The rapid dissolution from the matrix will likely accelerate the mechanism transition from initial dissolution to long-term diffusion with the formation of the passivation film due to the dissolution-surface reorganization or dissolution-reprecipitation mechanisms, as shown in Figure 7c-d. This can be supported by a

359 previous static leaching test conducted on $Ca(U_{0.5}Ce_{0.25}Hf_{0.25})_2Ti_2O_7$ by Xu et al. (2004), who
360 observed the formation of an amorphous Ti enriched layer [7]. The continuous formation of a
361 surface passivation film results in the gradual reduction of the A-site element release rate,
362 denoted by the transition stage from day 2 to day 6. The long-term dissolution up to 14-day
363 testing is dominated by the diffusion controlled stage through the dense passivation film when
364 fully covering on the sample surface.

365 **4. Impact of structural/material parameters on chemical durability**

366 The initial rate and long-term rate of the A-site elements, and their correlation with mixing
367 entropy and chemical disorder can be found in Figures 8c-d. However, no clear trends can be
368 observed in both short time and long term release rates of the A-site cations with increased
369 entropy from binary, ternary, quaternary to high-entropy compositions with or without uranium
370 incorporation. The highest elemental release rate of A-site cations for $(Sm,Yb,Gd)_2Ti_2O_7$ and
371 $(Sm,Yb,Gd,U)_2Ti_2O_7$ cannot be explained simply by entropy variation. In our previous study,
372 mixing entropy itself cannot be used to explain the variation of thermal conductivity in
373 multicomponent Ti-pyrochlore solid solutions due to the strong lattice distortion, leading to the
374 variation in phonon scattering [26]. Similar strong atomic displacement and lattice distortion of
375 high-entropy rare-earth niobates were also revealed by Wright (2022) due to the increased size
376 mismatch [49]. Different from high-entropy alloys with a relatively simple crystalline structure,
377 the strong chemical disorder accompanying with the lattice distortion and variation in the oxygen

sublattice for multicomponent Ti-pyrochlore solid solution may significantly impact the chemical durability instead of mixing entropy, which has not been reported previously.

A strong correlation in the dissolution rate of mono-component pyrochlore with ionic radius of the A-site cation was reported, in which materials display improved corrosion resistance for smaller-sized lanthanide pyrochlores, consistent with the increased strength in the RE-oxygen bonds [48]. Compared to the single component Ti-pyrochlore, the single phase Ti-pyrchlore solid solution has greater chemical disorder through strong atomic displacement and lattice distortion, exhibiting complex mechanisms that govern the chemical durability than the mixing entropy. Therefore, to further elucidate the dominant factors in governing the dissolution behavior of multicomponent titanate solid solutions, the correlations in the short-term and long-term release rates of the A-site cations with chemical disorder (size disorder and mass disorder) and mixing entropy are identified and shown in Figure 8 and 9. A negative correlation with high fitting coefficient between chemical disorder (size or mass) and A-site release rate can be observed, except for the long-term release rate for mass disorder as shown in Figure 8a and 8b. This is consistent with the previous research by Wright (2021), supporting the idea that chemical disorder plays an important role in structure and chemical stability. Meantime, a moderately negative correlation can be observed for mixing entropy, especially for the short-term A-site release rate, which indicates the mixing entropy might not dominate the chemical durability of the multi-component pyrochlore solid solution, as shown in Figure 8c [26]. Notably, the

correlation coefficient can be significantly reduced for both chemical disorder and mixing entropy by including the $(Yb,U)_2Ti_2O_7$, as shown in Figure 9. The weak correlation by taking consideration of $(Yb,U)_2Ti_2O_7$ might be attributed to the large atomic weight and Shannon ionic radii of U^{4+} as compared to Yb^{3+}. Specifically, the shannon ionic radii for an 8-coordinated U^{4+} are 1.14 Å, respectively), larger that that of Yb^{3+} (shannon ionic radii for an 8-coordinated and 6-coordinated Yb^{3+} are 1.125 Å) . As a results, the mixing entropy, size disorder and mass disorder of the corresponding ($(Yb,U)_2Ti_2O_7$) are 1.49, 0.26% and 5%, respectively (Supplemental Table s2), which are lower than these of other multi-component pyrochlore solid solutions, leading to the misfitting of the curves as demonstrated in the Figure 8 and 9. Thus, the incorporation of a small amount of uranium can lead to a large size disorder and mass deviation from that of the multicomponent solid solutions without uranium incorporation, which cannot be simply reflected by mixing entropy effect. For instance, the calculated mass disorder for $(Yb,U)_2Ti_2O_7$ and $(Sm,Gd,Yb,U)_2Ti_2O_7$ is determined as 5% and 23% separately; while the mass disorder for the undoped $(Sm,Yb)_2Ti_2O_7$ and $(Sm,Gd,Yb)_2Ti_2O_7$ are only 7.4% and 8.1%, respectively. The incorporation of smaller-sized rare-earth elements (reduction of the cationic ionic radius ratio) and tetravalent uranium increase the tendency of the structural transition from more ordered pyrochlore towards defect fluorite, and likely alter the bonding environment of the A-O and B-O polyhedrons, significantly impacting the chemical durability.

On the other hand, the short term and long term uranium release rate itself can be well

associated with either chemical disorder or mixing entropy. Similar with A-site release rate, the $(Yb,U)_2Ti_2O_7$ seems to be an outliner in the fitting curves, especially for size disorder, which can be attributed to the incorporation of much heavier and large ionic radii U into the lattice leading to the significant distortion in the size, mass and entropy. However, the discrepancy of U release rates between short-term and long-term was observed which further implies a potential mechanism beyond lattice distortion exist. The fast A-site element dissolution and surface alteration for binary and ternary U-incorporated Ti pyrochlore induce the simultaneous surface reorganization and gradually growth of passivation film, delaying the uranium dissolution, by acting as a protective layer as denoted in Figure 7d and Figure 10. Therefore, the dissolution behavior of multi-component pyrochlore solid solution is not intrinsic, displaying a strong microstructure dependence. The long-term U release rate in the high-entropy pyrochlore solid solution as compared to the literature data can be further seen in Figure 10d. The high-entropy pyrochlore shows significantly-low U release rate and much better chemical durability than single component pyrochlore, zirconolate or iron phsosphate glass even in aggressive acidic solutions, further implying its potential application in the nuclear waste form [7,51,52,53]. It is of worthy noting that different testing protocols have a significant impact on the uranium dissolution rate. In this work, we performed an aggressive leaching test (ASTM C1280) to accelerate the evaluation of the chemical durability of the sample coupons herein with nitric acid acted as the dissolution agent as pyrochlore in generally is highly corrosion resistant. For

435 comparison, a PCT test was carried out to appraise the chemical durability of zirconia, SYNROC
436 or (Ca,U)$HfTi_2O_7$ with deionized water acted as an agent [7,51,52,53]. The significantly lower
437 uranium release rate for high-entropy pyrochlore in this study by accelerated corrosive testing as
438 compared to the conventional U-bearing waste form (Ti-pyrochlore, SYNROC, cubic zirconia or
439 pron phosphate glas) suggests the robust chemical durability of the high-entropy pyrochlore solid
440 solution, which facilitates its application in the nuclear waste geological repository (Figure 10d).

441 In summary, the chemical disorder, especially the size disorder, appears to be an effective
442 indicator for the prediction of chemical durability for multicomponent Ti-pyrochlore solid
443 solutions. The deviation of chemical durability indicates that mixing configurational entropy may
444 not be ideal as a descriptor in correlating the chemical durability of multicomponent oxide solid
445 solutions with or without uranium incorporation. The study herein implies the elemental
446 dissolution behavior and chemical durability can possibly be tailored by tuning its chemical
447 disorder with the ionic size difference, which has a strong impact on the lattice distortion. A
448 detailed understanding of how composition complexity associated with multiple cation
449 substitutions affecting the chemical disorder, and structural characteristics (particularly structural
450 transition from ordered pyrochlore to defect fluorite and the variation of oxygen vacancies at the
451 8a site) is essential to reveal the underlying mechanisms and key structural parameters governing
452 the corrosion behavior of multicomponent pyrochlore solid-solutions. Nevertheless, the chemical
453 and size disorder appears to be a robust indicator for representing the chemical durability

behavior of multicomponent Ti-pyrochlore solid solutions. This will be helpful for guiding material design with desired thermal and chemical behavior for the nuclear waste forms with comparable or even lower radionuclide release rates as compared to the state-of-art nuclear waste forms, e.g., SYNROC, zirconia, iron phosphate, etc.

5 Conclusions

In this work, single-phase multicomponent Ti-pyrochlore solid solutions with and without uranium incorporation were fabricated via solid-state reaction and sparking plasma sintering, and their chemical durability was evaluated by accelerated semi-dynamic leaching testing. Both short and long term dissolution rates were measured by solution chemistry analysis and the microstructure evolution of pyrochlore solid solutions was characterized. A transition in dissolution mechanisms can be observed from incongruent dissolution with preferential release of A-site element to preferential release of Ti. Of particular interest, the incongruent dissolution mechanism and the surface alteration-reorganization result in the formation of a Ti-enriched passivation film in high entropy pyrochlore composition. The heterogeneity of the A-site rare earth elemental (REE) release rates can be attributed to the strong chemical disorder and lattice distortion for the multicomponent Ti pyrochlore solid solutions. Mixing entropy alone cannot solely explain the heterogeneity of the chemical durability, and a strong positive correlation between size disorder and A-site release rate can be observed. For uranium-incorporated multicomponent solid solutions, the release rate of uranium gradually decreases with increased

entropy in the multicomponent compositions, and the tunable release rate of radionuclides implies great potential in designing advanced waste form materials with optimized performance for effective waste management by controlling chemical/structural disorder in compositionally complex materials.

Acknowledgment

The synthesis of the multicomponent titanate pyrochlore solid solutions was supported by NSF under the Award DMREF-2119423. The dissolution testing of the multicomponent pyrochlore solid solution was supported as part of the Center for Performance and Design of Nuclear Waste Forms and Containers (WastePD), an Energy Frontier Research Center (EFRC) funded by the U.S. Department of Energy, Office of Science, Basic Energy Sciences under Award DE-SC0016584. The TEM characterization was supported by Laboratory Directed Research and Development (LDRD) (21A1050-075FP) project of Idaho National Laboratory (INL) which is operated by U.S. Department of Energy, Office of Nuclear Energy under DOE Idaho Operations Office Contract DE-AC07-05ID14517.

Data Availability

The data will be available upon request. Please contact the corresponding author if you need any further assistance.

Reference

1. Zhang K.B., He Z.S., Peng L., Zhang H.B., Lu X.R. Self-propagating synthesis of $Y_{2-x}Nd_xTi_2O_7$ Pyrochlore and its aqueous durability as nuclear waste form. Scripta Materialia, 146(2018)300-303.

2. Jafar M., Sengupta P., Achary S.N., Tyagi A.K. Phase evolution and microstructural studies in $CaZrTi_2O_7$ (zirconolite)-$Sm_2Ti_2O_7$(Pyrochlore) system. Journal of European ceramic society, 34

(2014) 4373-4381.

3. Ringwood A.E., Oversby V.M., Kesson S.E., Sinclair W., Ware N., Hibberson W., Major A. Immobilization of high-level nuclear reactor wastes in SYNROC: A current appraisal. Nuclear and chemical waste management. 2(1981)287-305.

4. Yudintsev R.S.V., Stefanovsky S.V., Nikonov B.S. A Pyrochlore based matrix for isolation of the REE-Actinide fraction of wastes from spent nuclear fuel reprocessing. Geochemistry, 454 (2014) 211-215.

5. Yang J.W., Tang B.L., Luo S.G. Pyrochlore-rich Synroc as a host for immobilization of actinides. Mat. Res. Soc. Symp. Proc., 663 (2001) 1-8.

6. Kong L.G., Zhang Y.J., Karatchevtseva I. Preparation of $Y_2Ti_2O_7$ pyrochlore glass-ceramics as potential waste forms for actinides: the effects of processing conditions. Journal of Nuclear Materials, 494 (2017) 29-36.

7. Xu H.F., Wang Y.F., Zhao P.H., Bourcier W.L., Konynenburg R.V., Shaw H.F. Investigation of pyrochlore-based U-Bearing ceramic nuclear waste: uranium leaching test and TEM observation. Environmental Science and Technology, 38 (2004) 1480-1486.

8. Farmer J.M., Boatner L.A., Chakoumakos B.C., et al. Structural and crystal-chemical properties of rare-earth titanate pyrochlores. Journal of alloys and compounds, 605 (2014) 63-70.

9. Shu X.Y., Qing Q., Li B.S., et al. Rapid immobilization of complex simulated radionuclides by as-prepared $Gd_2Zr_2O_7$ ceramics without structural design. Journal of nuclear materials, 526 (2019) 1-8.

10. Zhang K.B., Wen G.J., Zhang H.B., et al. Self-propagating high-temperature synthesis of $Y_2Ti_2O_7$ Pyrochlore and its aqueous durability. Journal of nuclear materials, 465 (2015) 1-5.

11. Hippel F.V., Ewing R.C., Garwin R., Macfarlane A. Time to bury plutonium. Nature, 485(2012)167-168.

12. Wang J., Wang J.X., Zhang Y.B., et al. Flux synthesis and chemical stability of Nd and Ce co-doped $(Gd_{1-x}Nd_x)2(Zr_{1-x}Ce_x)_2O_7$ (0<x<1) pyrochlore ceramics for nuclear waste forms. Ceramic International, 43 (2017) 17064-17070.

13. Gild J., Samiee M., Braun J.F., Harrington T., Vega H., Hopkins P.E., Vecchio K., Luo J. High entropy fluorite oxides. J. Eur. Ceram. Soc., 38(2018)3578-3584

14. Wright A.J., Wang Q.Y., Ko S.T., Chung K.M., Chen R.K., Luo J. Size disorder as a descriptor for predicting reduced thermal conductivity in medium and high entropy pyrochlore oxides. Scr. Mater., 181 (2020)76-81

15. Wright A.J., Luo J. A step forward from high entropy ceramics to compositionally complex ceramics: a new perspective. J. Mater. Sci., 274 (2020)1-31

16. Peng L., Zhang K.B., He Z.S., Yin D., Xue J.L., Xu C., Zhang H.B. Self-propagating high temperature synthesis of ZrO2 incorporated $Gd_2Ti_2O_7$ pyrochlore. Journal of advanced ceramics, 7(2018)41-49.

17. F. Li, L. Zhou, J.X. Liu, Y.C. Liang, G.J. Zhang. High entropy pyrochlores with low thermal conductivity for thermal barrier coating materials. J. Adv. Ceram., 8 (2019), pp. 576-582

18. Lian J., Helena K.B., Kennedy B.J., et al. effect of structure and thermodynamic stability on the response of lanthanide stannate pyrochlores to ion beam irradiation. Journal of Physical Chemistry B., 110 (2006) 2343-2350.

19. Shlyakhtina A.V., Sokolov A.E., UIyanov V.A., et al. neutron diffraction investigation of the evolution of the crystal structure of oxygen conducting solid solutions $(Yb_{1-x}Ca_x)_2Ti_2O_7$ (x=0, 0.05, 0.1). Structure of inorganic compounds, 54 (2009) 25-30.

20. Wang J., Wang J.X., Zhang Y.B., et al. Flux synthesis and chemical stability of Nd and Ce co-doped $(Gd_{1-x}Nd_x)2(Zr_{1-x}Ce_x)_2O_7$ (0<x<1) pyrochlore ceramics for nuclear waste forms. Ceramic International, 43 (2017) 17064-17070.

21. Ewing R.C., Weber W.J., Lian J. Nuclear waste disposal-pyrochlore ($A_2B_2O_7$): nuclear waste

545 form for the immobilization of plutonium and “minor” actinides. Journal of applied physics, 95
546 (2004) 5949-5971.
547 22. Patwe S.J., Katari V., Salke N.P., et al. Structural and electrical properties of layered
548 perovskite type Pr2Ti2O7: experimental and theoretical investigations. Journal of materials
549 chemistry C, 3 (2015) 4570-4584.
550 23. Liu D.B., Shi B.L., Geng L.Y. High-entropy rare-earth zirconate ceramics with low thermal
551 conductivity for advanced thermal-barrier coatings. Journal of Advanced ceramic society,
552 11(2022)961-973.
553 24. Chen Y.Y., Qi J.L., Zhang M.H. Pyrochlore-based high-entropy ceramics for capacitive
554 energy storage. Journal of Advanced ceramics, 11(2022)7.
555 25. Wang Z.J., Zhou G.H., Jiang D.Y., Wang S.W. Recent development of A2B2O7 system
556 transparent ceramics. Journal of Advanced Ceramics, 7(2018)289-306.
557 26. Yang K., Bryce K., Zhu W.G., Zhao D., Lian J. Multicomponent pyrochlore solid solutions
558 with uranium incorporation – A new perspective of materials design for nuclear applications.
559 Journal of the European Ceramic Society, 41(2021)2870-2882.
560 27. Yang K., Lei P.H., Yao T.K., Gong B.W., Wang Y.C., Li M.X., Lian J. A systematic study of
561 lanthanide titanates ($A_2Ti_2O_7$) chemical durability: corrosion mechanisms and control parameters.
562 Corrosion Science, 185(2021)109394.
563 28. Yang K., Wang Y.C., Lei P.H., Zhao D., Lian J. Chemical durability and surface alteration of
564 lanthanide zirconates (A2Zr2O7: A = La-Yb). Journal of the European Ceramic Society,
565 41(2021)6018-6028.
566 29. BraunJ.L., Rost, M. Lim, A. Giri, D.H. Olson, G.N. Kotsonis, G. Stan, D.W. Brenner, J.P. M
567 aria, P.E. Hopkins. Charge-induced disorder controls the thermal conductivity of
568 entropy-stabilized oxides. Adv. Mater., 30 (2018)1805004.
569 30. Yu T.H., Tuller H.L. Electrical Conduction and Disorder in the Pyrochlore System
570 (Gd1xCax)2Sn2O7. J. Electroceram., 2(1998)49–55 .

31. Yu T.H., Tuller H.L. Ionic Conduction and Disorder in the Gd2Sn2O7 pyrochlore System. Solid State Ionics, 86–88 (part 1) (1996)177–182 .

32. Chen Y.H., Kanan M.W. Tin Oxide Dependence of the CO2 Reduction Efficiency on Tin Electrodes and Enhanced Activity for Tin/Tin Oxide Thin-Film Catalysts. Journal of American chemistry society, 134(2012)1986-1989.

33. Park S., Hwang H.J., Moon J. Catalytic Combustion of Methane Over Rare Earth Stannate Pyrochlore. Catal. Lett., 87(2003)219–223 .

34. Moon J., Awano M., Maeda K, Hydrothermal Synthesis and Formation Mechanisms of Lanthanum Tin Pyrochlore Oxide. J. Am. Ceram. Soc., 84 (2001)2531–2536 .

35. Mao Y., Li G., Xu W., Feng S, Hydrothermal Synthesis and Characterization of Nanocrystalline Pyrochlore Oxides M2Sn2O7 (M = La, Bi, Gd or Y). J. Mater. Chem., 10 (2000)479–482.

36. ASTM-C1308-08, accelerated leach test for diffusive releases from solidified waste and a computer program to model diffusive, fractional leaching from cylindrical waste forms, ASTM International, west Conshohocken, PA, 2009.

37. Cote P.L., Constable T.W., Moreira A.J.N. An evaluation of cement-based waste forms using the results of approximately two years of dynamic leaching. Nuclear and Chemical Waste Management, 7(1987)129-139.

38. Wan C.L., Qu Z.X., Du A.B., Pan W. (2011). Order-disorder transition and unconventional thermal conductivities of the (Sm1-x,Ybx)2Zr2O7 series. Journal of American Ceramic Society, 94(2011)592-596.

39. Liu K., Zhang K.B., Deng T., Zheng J.J., Luo B.Z., Zhang H.B. Grain size effects on the aqueous durability of Gd2Zr2O7 ceramics as high-level radioactive wastes matrix and its leaching mechanism. Ceramic International, 47(2021)13363-13373.

40. Du M.R., Liu S.X., Ge Y.F., Li Z.P., Wei T., Yang X., Dong J.J. Preparation and effect of grain size on the thermal stability, phase transition, mechanical property, and photocatalytic

property of pyrochlore (La0.2Nd0.2Sm0.2Gd0.2Y0.2)2Zr2O7 high-entropy oxide.Ceramic International, 12(2022)12434-12442.

41. Han Y.J., Yu R.W., Liu H.H., Chu Y.H. Synthesis of the superfine high-entropy zirconate nanopowders by polymerized complex method. Journal of Advanced Ceramics, 11(2022)136-144.

42. Wang Y.F., Yang F., Xiao P. Role and determining factor of substitutional defects on thermal conductivity: A study of $La_2(Zr_{1-x}B_x)_2O_7$ (B=Hf,Ce, $0\leq x\leq 0.5$) pyrochlore solid solutions. Acta Materialia, 68(2014)106-115.

43. Zhang Z.M., Blackford M.G., Lumpkin G.R., Smith K.L., Vance E.R. Aqueous dissolution of perovskite ($CaTiO_3$): Effect of surface damage and Ca in the leachant. Journal of Materials Research, 20(2005)2462-2473.

44. Gong B.W., Yang K., Lian J., Wang J.W. Machine Learning-enabled Prediction of Chemical Durability of A2B2O7 Pyrochlore and Fluorite. Computational Materials Science, 200(2021)110820.

45. Lasaga A., Luttge A. Variation of crystal dissolution rate based on a dissolution step wave model. Science, 291 (2001) 2400-2404.

46. Finkelstein S., Brandt F., Rozov K., et al. Dissolution of ZrO_2 based pyrochlores in the acid pH range: a macroscopic and electron microscopy study. Applied Geochemistry, 49(2014) 31-41.

47. Zhang Y. Hart K.P., Blackford M.G., et al. durability of pyrochlore-rich titanate ceramics designed for immobilization of surplus plutonium. Mat. Res. Soc. Symp. Proc. 663 (2001) 1-8.

48. Leturcq G., McGlinn P.J., Barbe C., et al. Aqueous alteration of nearly pure Nd-doped zirconolite ($Ca_{0.8}Nd_{0.2}ZrTi_{1.8}Al_{0.2}O_7$), a passivating layer control. Applied Geochemistry, 20(2005) 899-906.

49. Popov V.V., Menushenkov A.P., Ivanov A.A., et al. A XAFS investigation of amorphous to crystalline and fluorite to pyrochlore phase transitions in $Ln_2M_2O_7$ (Ln=Gd, Tb, Dy; M=Ti, Zr). Radiation physics and chemistry,175(2020)1-5.

623 50. Wright A.J., Wang Q.Y., Yeh Y.T., Zhang D.W., Everett M., Luo J. Short-range order and
624 origin of the low thermal conductivity in compositionally complex rare earth niobates and
625 tantalates. Acta Materialia, 235(2022)118056.

626 51. Yang J.W., Tang B.L., Luo S.G. Pyrochlore-Rich Synroc as a Host for Immobilization of
627 Actinides. MRS Proceeding, 663(2000)333.

628 52. Burakov B., Anderson E., Yagovkina M. Behavior of Pu-doped ceramics based on cubic
629 zirconia and pyrochlore under radiation damage. Journal of nuclear science and technology,
630 39(2002)733-736.

631 53. Danilov S.S., Vinokurov S.E., Stefanovsky S.V., Myasoedov B.F. Hydrolytic Durability of
632 Uranium-Containing Sodium Aluminum (Iron) Phosphate Glasses. Radiochemistry,
633 59(2017)226-229.

634
635
636

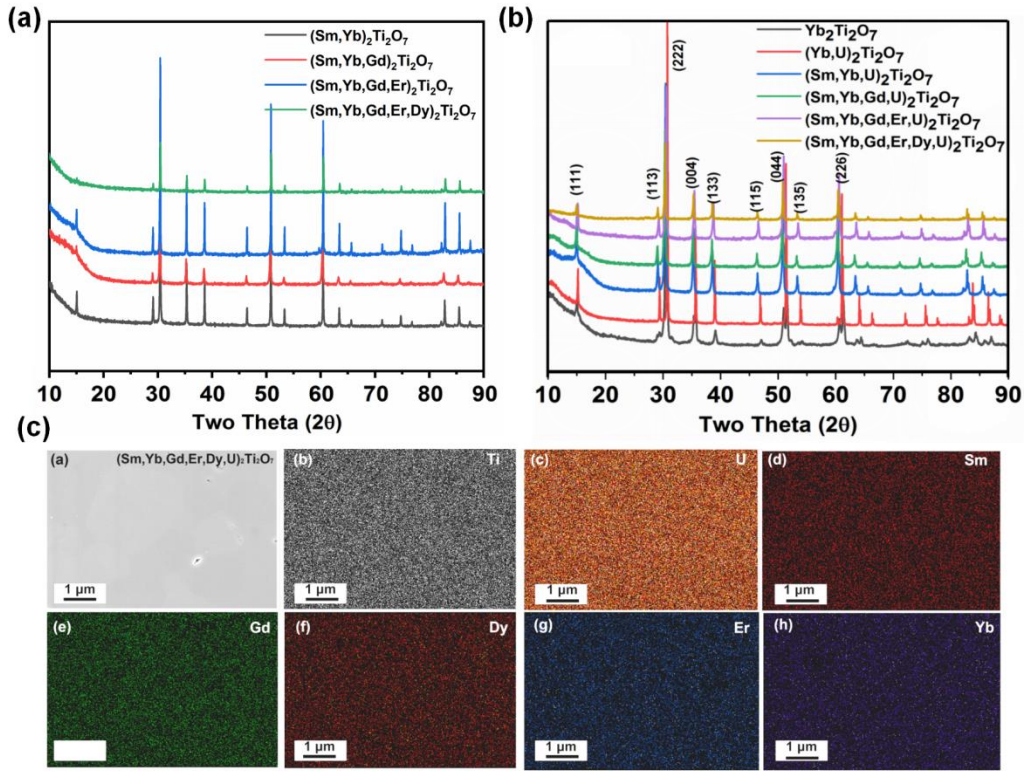

637

638 **Fig. 1** (a,b) XRD patterns of the as-fabricated titanate pyrochlore solid solutions with and without
639 uranium incorporation; and (c) Surface microstructure and elemental mappings of the
640 $(Sm,Yb,Gd,Er,Dy,U)_2Ti_2O_7$ (c).

641

642

643

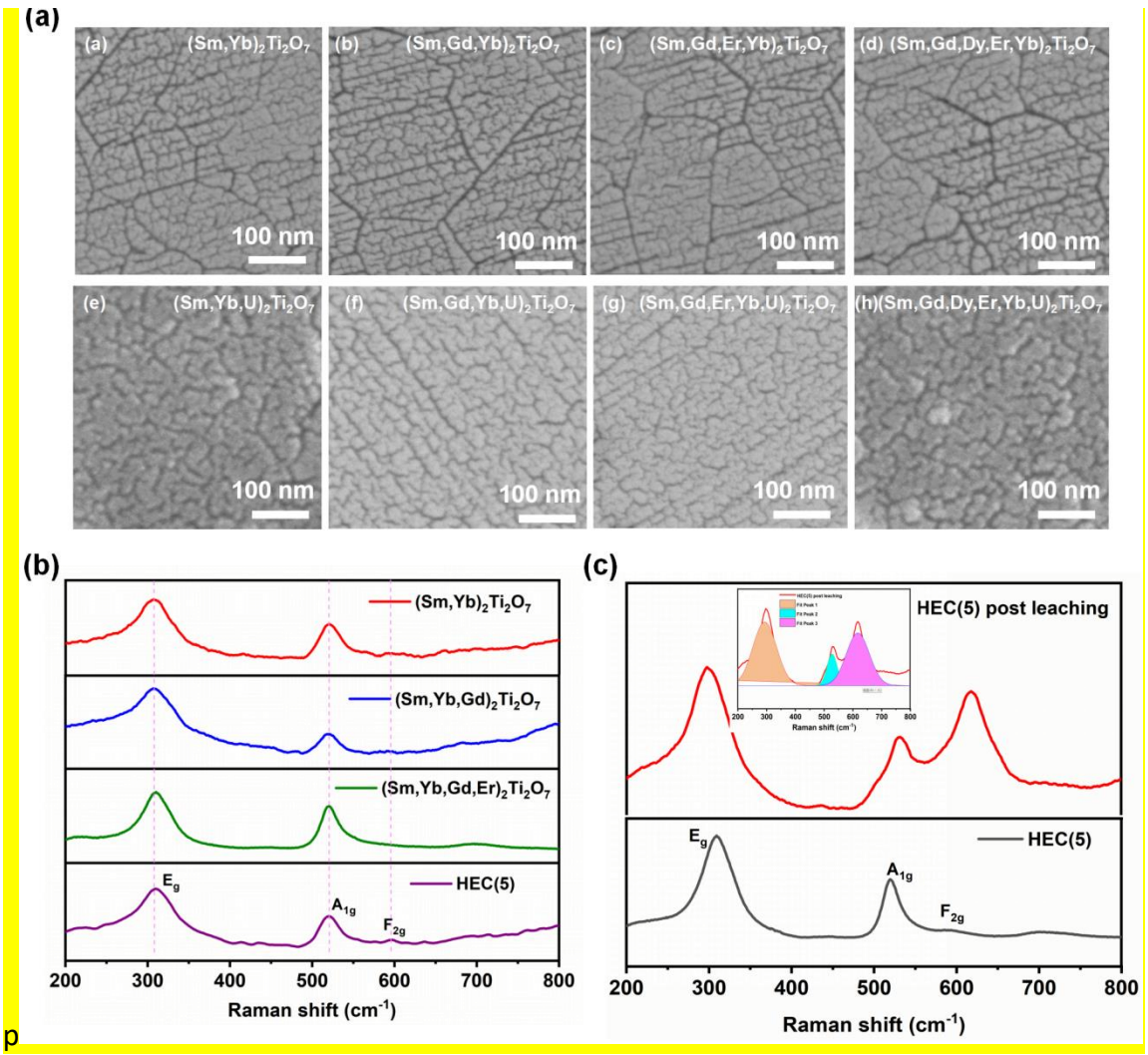

p

Fig. 2 (a) Surface microstructure of the multicomponent titanate pyrochlore solid solutions post 14-days' leaching test in nitric acid aqueous solution (pH = 1, 90 ºC); (b) Corresponding Raman spectra of the Ti-pyrochlore solid solutions; (c) Raman shift of the high-entropy Ti-pyrochlore before and post 14-days' leaching test .

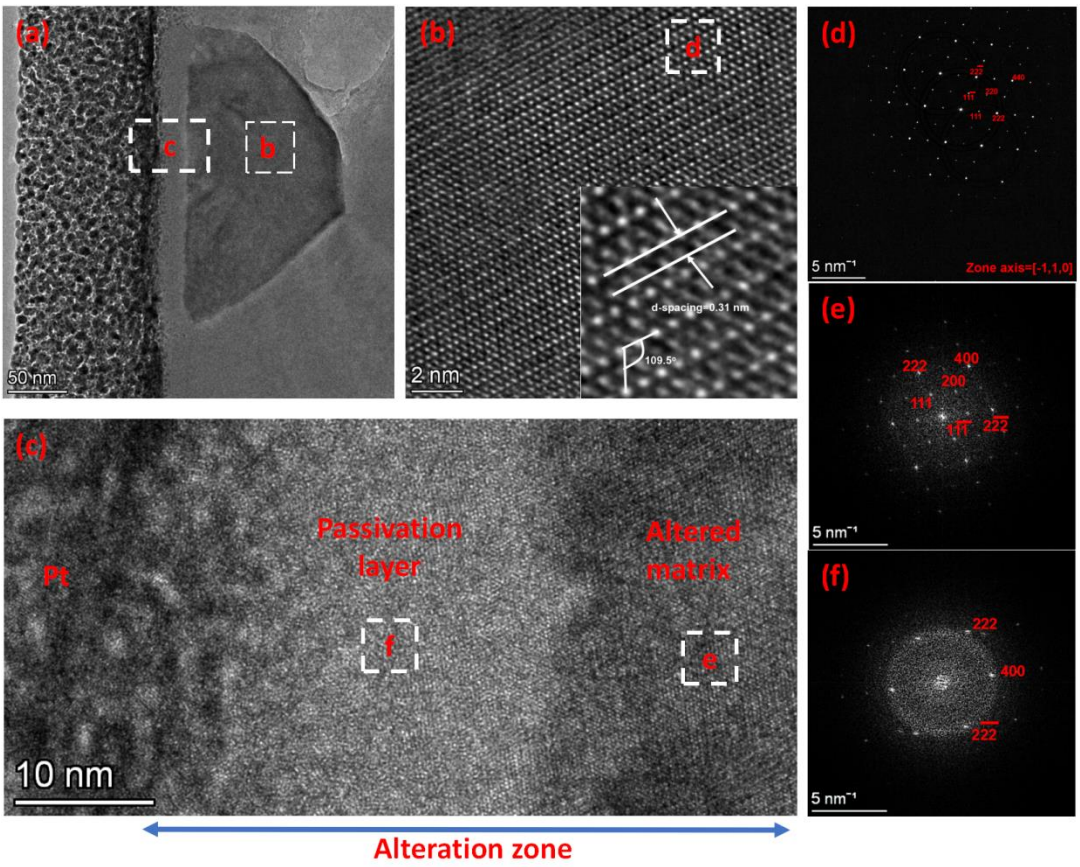

Fig. 3 STEM analysis of the surface alteration layer of the high-entropy Ti-pyrochlore post 14-days' leaching test: (a) a bright-field image across the top alteration layer; (b) a high-resolution STEM image of the crystalline grains underneath the top alteration layer; (c) a high-resolution STEM image of the top alteration layer; (d) a selected area electron diffraction pattern (SAED) of the crystalline grain underneath the top alteration layer; and (e-f) corresponding FFT patterns of the altered matrix and the alteration layer.

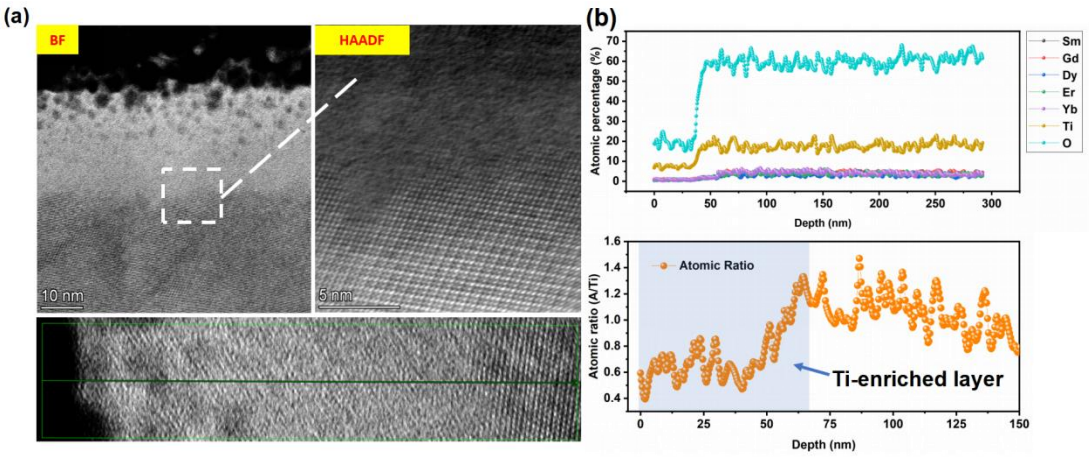

Fig. 4 STEM-EDS analysis of the top alteration layer of high-entropy Ti-pyrochlore: (a) STEM

analysis of the top alteration layer; and (b) corresponding elemental line scanning across the alteration layer.

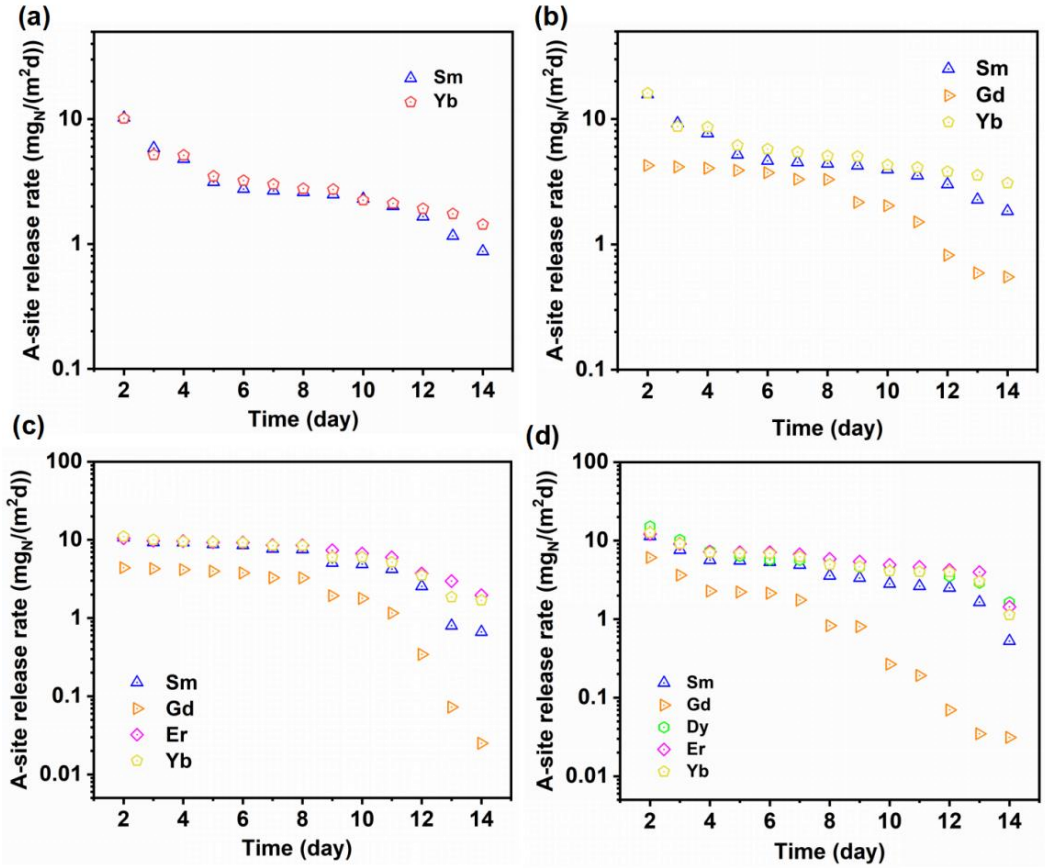

Fig. 5 Normalized elemental release rates of A-site cations of the Ti-pyrochlore solid solutions without uranium incorporation for binary, ternary, quaternary and high entropy solid solution (a-d).

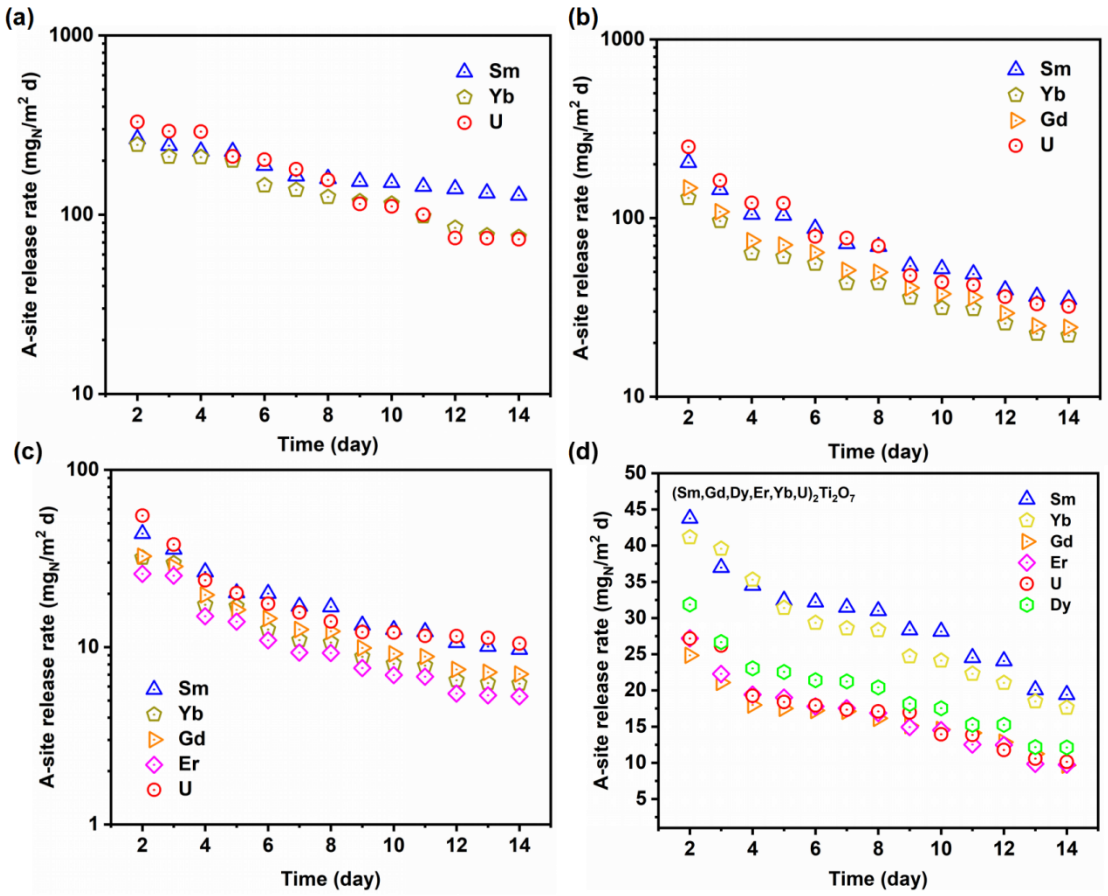

668

669 **Fig. 6** Normalized elemental release rates of A-site cations in the uranium-incorporated
670 Ti-pyrochlore solid solutions (a-d).

671

672

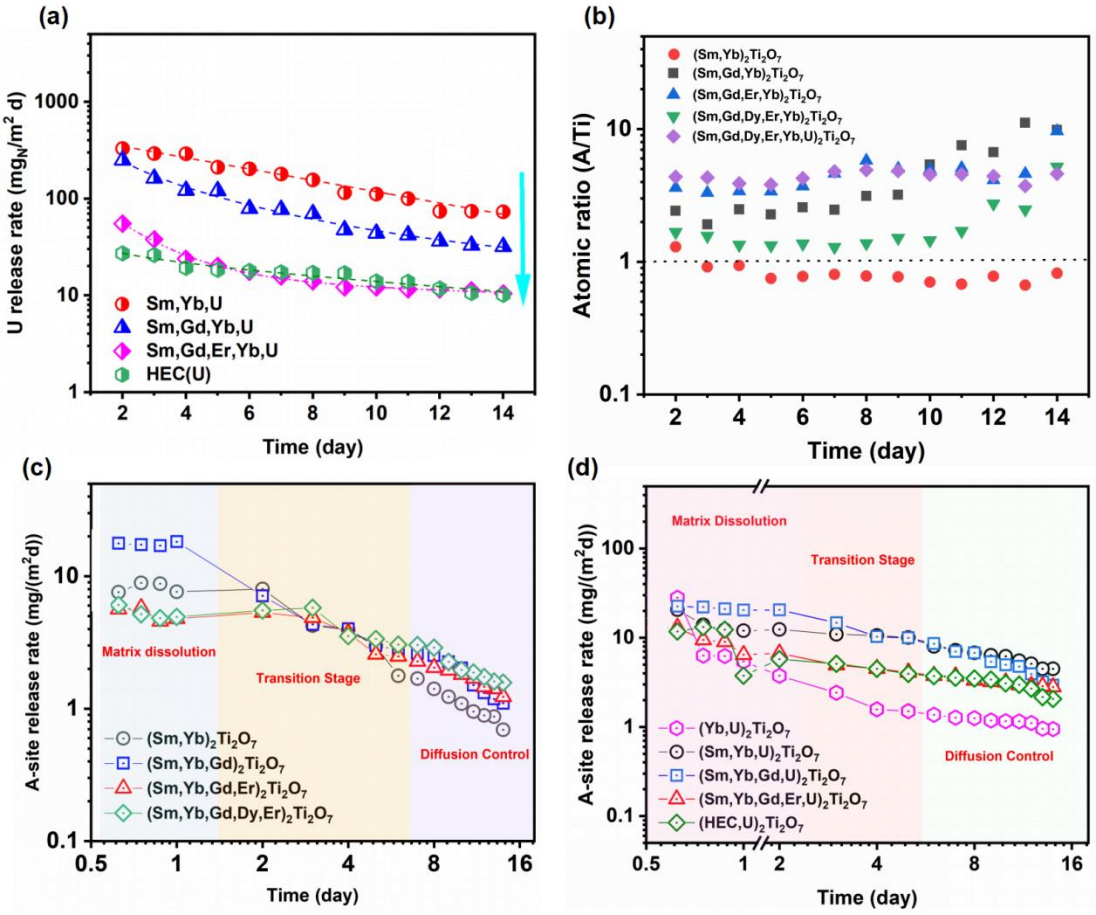

Fig. 7. Sum of the dissolution rates of the A-site cations for Ti-pyrochlore solid solution ($A_2Ti_2O_7$) for both short-term (1-day) and long-term (up to 14-days): (a) Normalized release rates of uranium from multicomponent titanate pyrochlore solid solutions; (b) Atomic ratios (A/Ti) of the A-site cation *vs*. Ti; and (c) multicomponent solid solutions without uranium; (d) multicomponent solid solutions with uranium;

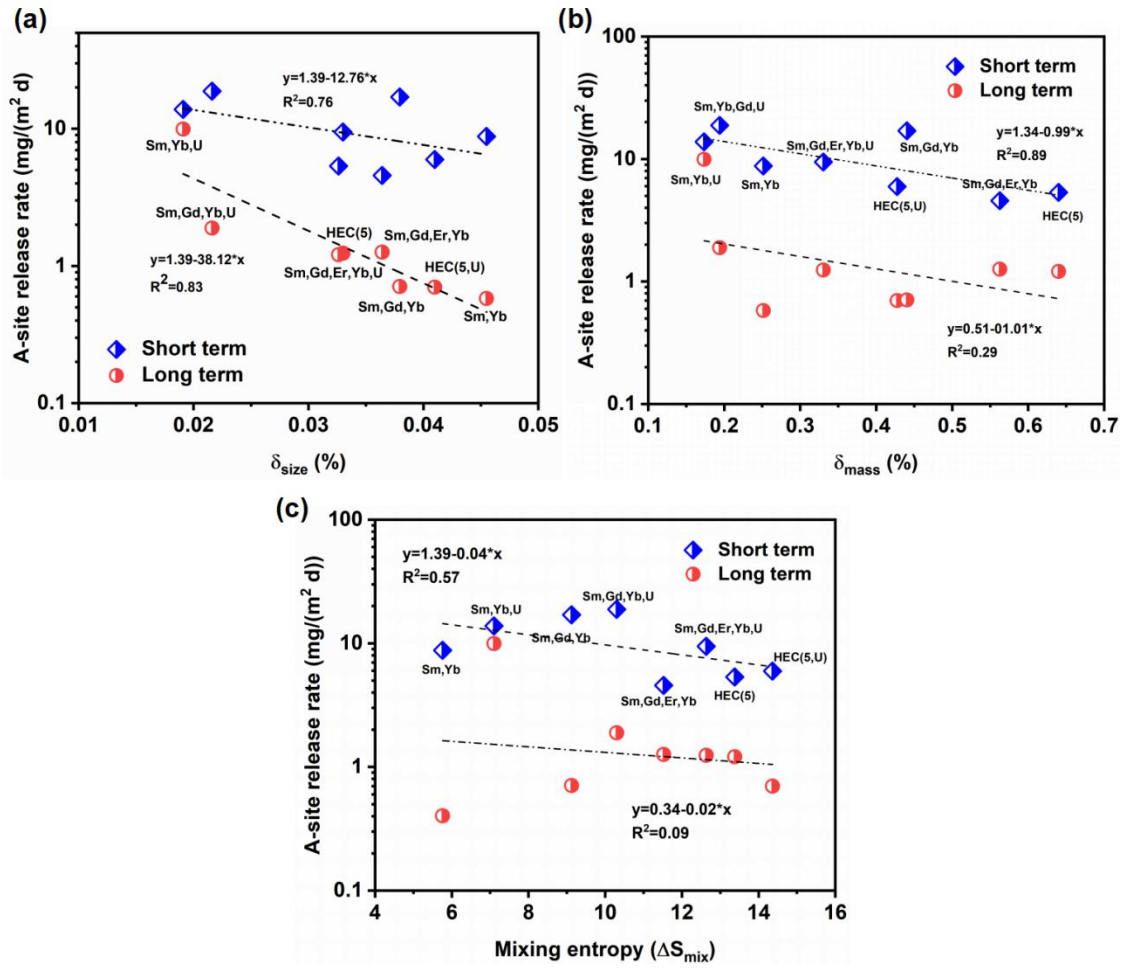

680

681 **Fig. 8** Sum of the initial rates and long term rates of the A-site cations of multicomponent titanate
682 pyrochlore solid solutions upon leaching testing in a nitric acid aqueous solution (pH = 1, 90 ºC),
683 and their correlations *vs.* size disorder (a), mass disorder (b), and mixing entropy (c).
684

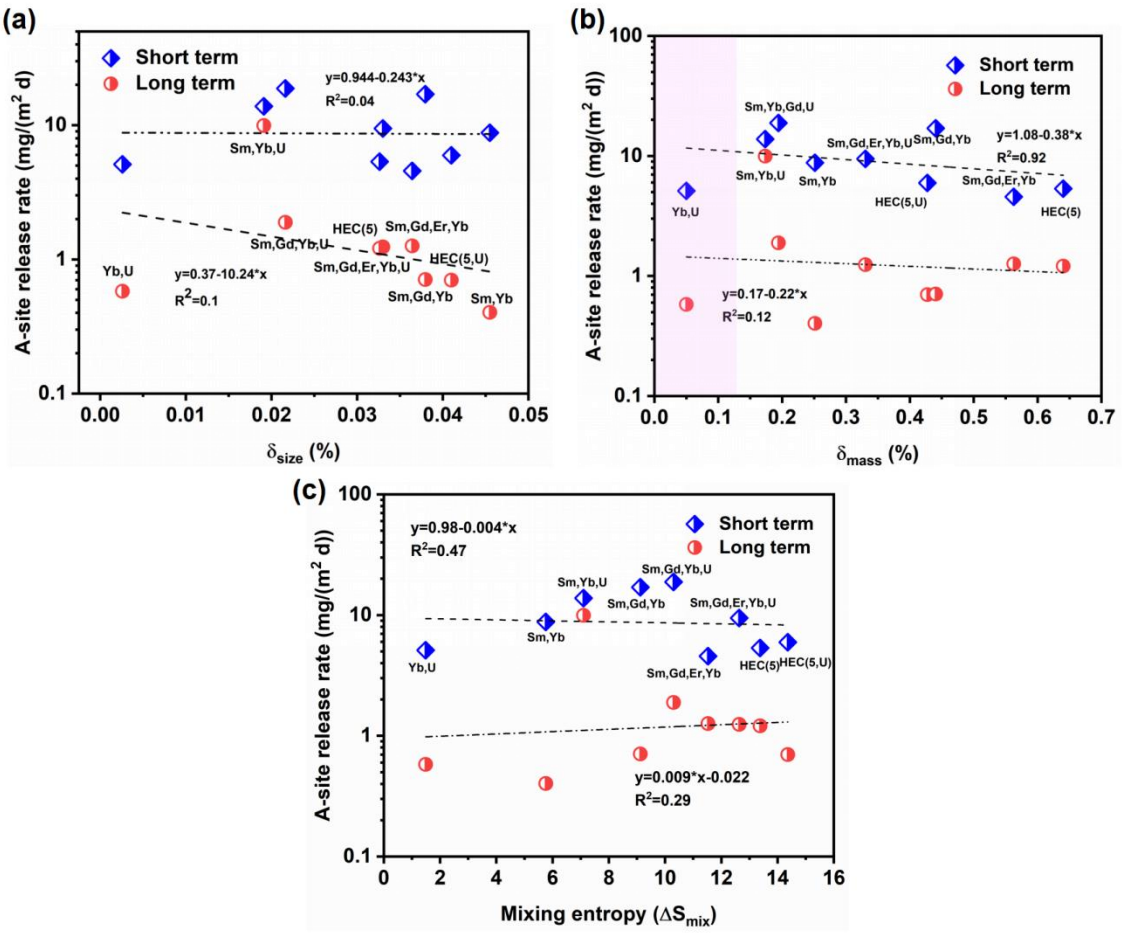

685

686 **Fig. 9** Sum of the initial rates and long term rates of the A-site cations of multicomponent titanate
687 pyrochlore solid solutions upon leaching testing in a nitric acid aqueous solution (pH = 1, 90 ºC),
688 and their correlations *vs.* size disorder (a), mass disorder (b), and mixing entropy (c).

689

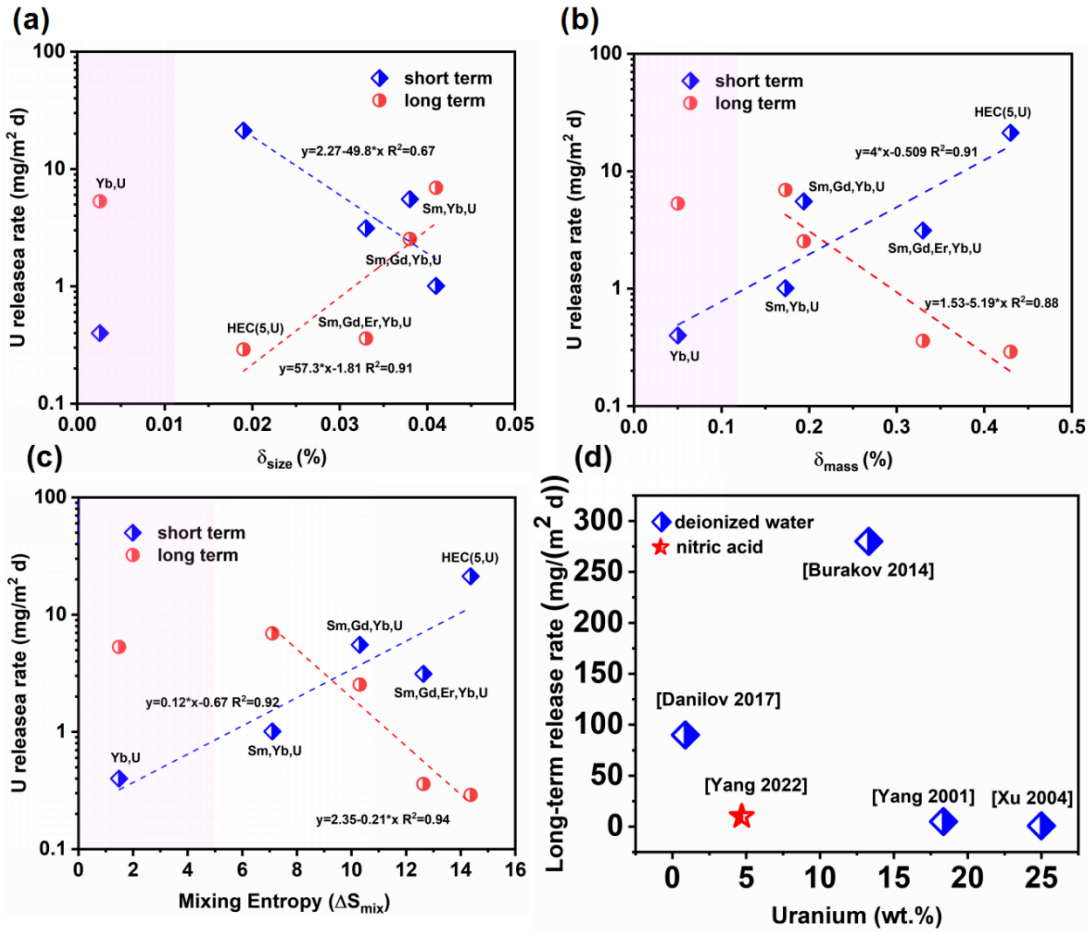

Fig. 10 Sum of the initial rates and long term rates of the uranium in multicomponent titanate pyrochlore solid solutions upon leaching testing in nitric acid aqueous solution (pH = 1, 90 ºC), and their correlations vs. size disorder (a), mass disorder (b), mixing entropy (c) and comparison with literature study.

Table 1 Short term and long term A-site elemental release rates of multicomponent pyrochlore solid solutions

	Sm,Yb	Sm,Yb,Gd	Sm,Yb,Gd,Er	HEC	Yb,U	Sm,Yb,U	Sm,Yb,Gd,U	Sm,Yb,Gd,Er,U	HEC,U
short term	8.8	17.0	4.6	5.4	5.1	13.8	18.8	9.5	6.0
long term	0.4	0.7	1.3	1.2	0.6	9.9	1.9	1.2	0.7

Supplemental Information:

Table S1 Cote's model fitting parameters of multicomponent pyrochlore solid solutions

	Sm,Yb	Sm,Yb,Gd	Sm,Yb,Gd,Er	HEC	Yb,U	Sm,Yb,U	Sm,Yb,Gd,U	Sm,Yb,Gd,Er,U	HEC,U
k_1	0.4	0.7	1.3	1.2	0.6	9.9	1.9	1.2	0.7
k_2	5.5	0.0	0	0	6.5	2.6	1.3	5.3	0
k_3	91.8	55.7	26.2	32.8	113.2	84.5	74.5	8.7E+01	1.2E+02
k_4	9.5	0.2	0.3	0.2	14.4	8.4E+00	10.5	1.2E+01	1.0E+02
R^2	1.0	1.0	1.0	1.0	1.0	8.9E-01	9.1E-01	9.5E-01	9.8E-01

Table S2 Chemical disorder and mixing entropy of multicomponent pyrochlore solid solutions

No.	size disorder	mass disorder	mixing entropy
(Sm,Yb)2Ti2O7	0.046	0.252	5.763
(Sm,Gd,Yb)2Ti2O7	0.038	0.441	9.125
(Sm,Gd,Er,Yb)2Ti2O7	0.036	0.563	11.526
(Sm,Gd,Dy,Er,Yb)2Ti2O7	0.033	0.640	13.381
(Yb,U)2Ti2O7	0.003	0.050	1.491
(Sm,Yb,U)2Ti2O7	0.019	0.173	7.103
(Sm,Gd,Yb,U)2Ti2O7	0.022	0.194	10.301
(Sm,Gd,Er,Yb,U)2Ti2O7	0.033	0.331	12.636
(Sm,Gd,Dy,Er,Yb,U)2Ti2O7	0.041	0.428	14.362

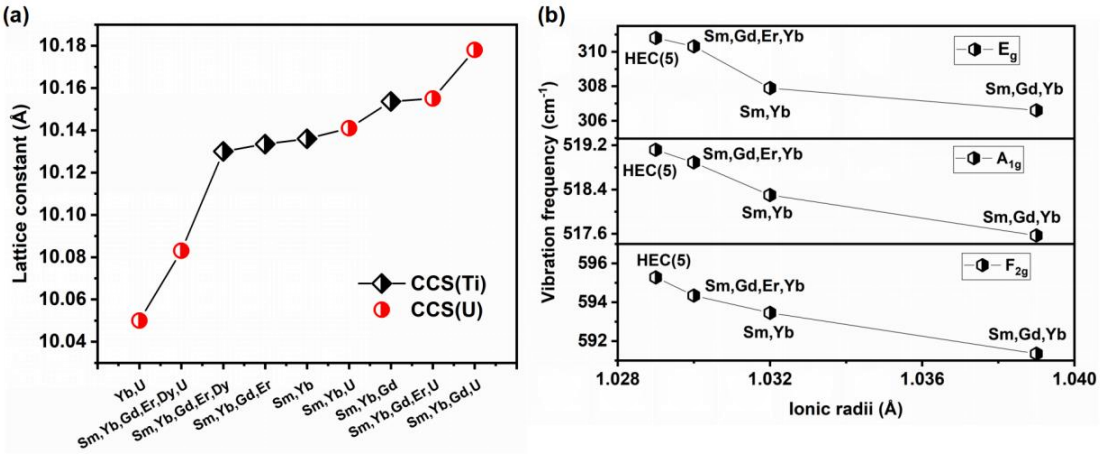

Fig.S1 Lattice constants derived from the corresponding XRD profiles (a); ionic radii versus Raman shift vibration frequency (b).

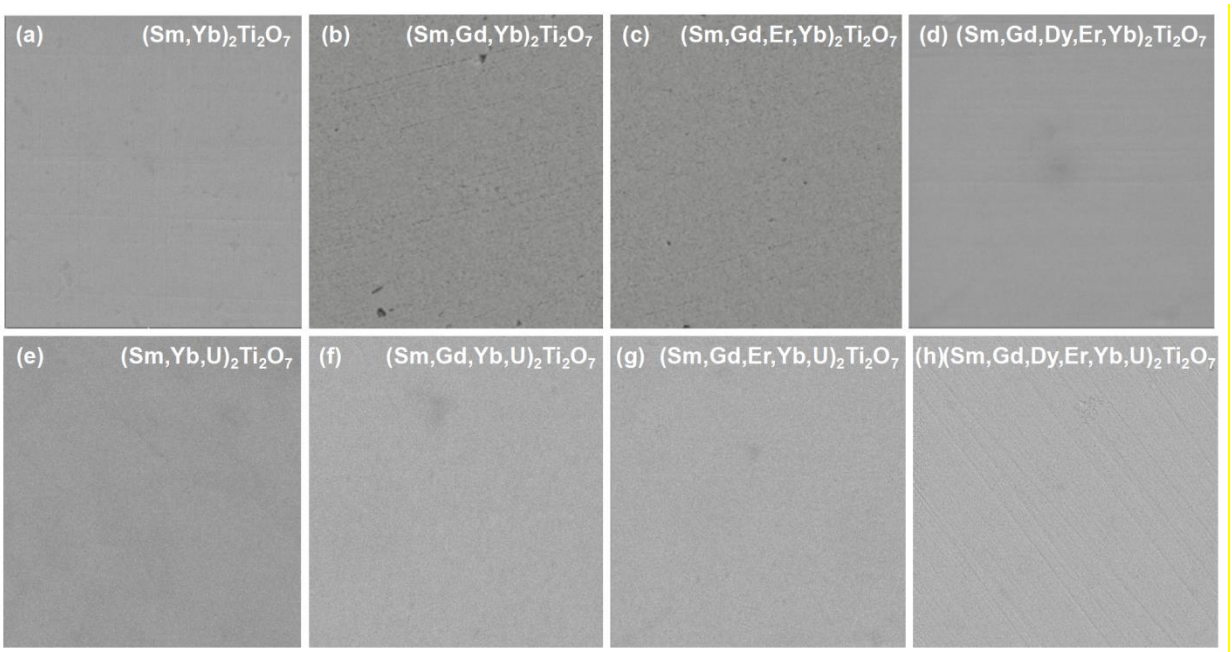

Fig.S2 Surface microstructure of the multicomponent titanate pyrochlore solid solutions before leaching tests.